Flat miniature heat pipe with sintered porous wick structure: experimental and mathematical studies

K. Zeghari, H. Louahlia

Flat miniature heat pipe with sintered porous wick structure: experimental and mathematical studies.

K. Zeghari, H. Louahlia

Normandy university, LUSAC Laboratory, Caen University

Site universitaire Bellevue, 120 rue de l'Exode – 50000 Saint-Lô. France

Abstract

Miniature heat pipes are considered as an innovative solution able to dissipate high heat fluxes with low working fluid charge, temperature control, and operating with minimum energy consumption and less noise. In this paper, results show that tilt ranging [10°:60°] has not an impact on heat transfer meanwhile the system thermal resistance is the lowest at horizontal position. A theoretical analysis on heat pipe thermal performance has been carried out based on experimental data by predicting heat pipe evaporation and condensation heat transfer coefficient. The measured heat transfer coefficients are close to the predicted results with a mean deviation less than 10%. A hydraulic mathematical model is developed and shows a good agreement with Kaya's study using water as working fluid. This work comprises a parametric study that investigates the effect of particles size, porosity, permeability, heat pipe length on heat transfer and capillary pressure. The obtained results show that the heat pipe operating temperature rises when particles size increases from 1μm to 90 μm and the optimum porosity range is between [10%-40%].

Key words: heat pipe, condensation, evaporation, porosity, cooling, heating, modelling

Corresponding author: hasna.louahlia@unicaen.fr

Phone:0233775518, Fax:0233771177

Nomenclature

A	Area, (m²)
C	permeability factor
Cp	Heat capacity, (J/kg.K)
db	equilibrium break-off diameter,(m)
e	Thickness,(m)
e_w	Thickness of heat pipe walls,(m)
g	Gravitational acceleration,(m/s²)
h	heat transfer coefficient, (W/m².K)
hlv	heat of vaporization, (J/kg)
L	Length, (m)
L_{eff}	Effective heat pipe length, (m)
M	Working fluid molar mass,(Kg/mol)
$\dot{m}$	Mass flow rate,(kg/s)
n	empirical exponent
P	Pressure, (Pa)
Pr	Prandtl number
Q	Heat transfer rate, (W)
R	Thermal resistance, (°C/W)
Re	Reynolds number
Reb	Reynolds number based on equilibrium break-off diameter
Red	Reynolds number based on Porous media particles diameter
Reff	Effective wick particles radius,(m)
R_g	Specific molar gas constant.
Rm	Meniscus radius,(m)
rs	Porous media particles radius,(m)
t	Height, (m)
T	Temperature, $(°C)$
U	Velocity,(m/s)
W	Width, (m)
z	Abscises, (m)

Greek symbols

α	Angle of heat pipe inclination,(°)
ϵ	Porosity, (%)
θ	Contact angle,(°)
λ	Thermal conductivity, (W/m.K)
λl	Thermal conductivity of pore fluid phase, (W/m.K)
λs	Thermal conductivity of pore solid phase, (W/m.K)
μ	Dynamic viscosity, (Pa/s)
ρ	Density, (kg/m^3)
σ	Surface tension, (N/m)

Subscripts

a	Adiabatic
amb	Ambient
cd	Condenser
conv	Convection
ct	Contact
e	Evaporator
eff	Effective
fin,b	Fins base
l	Liquid
opt	Optimum
sat	Saturation

sys	Heat pipe system	w	Wall
t	Total	wi	Wick
v	Vapor		

1. Introduction

Heat pipe is a passive cooling system which application extends from electronics cooling to building applications [1-3]. It is a closed device with high thermal conductivity which enables important amount of heat dissipation [4]. It comprises an evaporator which is in contact with the heating element, adiabatic region as it enables heat transport and a condenser that allows heat withdrawal. Heat pipes are characterized by achieving important heat transfer rates comparing to other common heat transfer devices thanks to internal working fluid phase change. Once a heat load is applied to the evaporator zone, the working volume contained in the heat pipe is vaporized and transferred to the condenser through the adiabatic region due to the pressure difference between the evaporator and condenser. The vapour is condensed by releasing heat to the condenser bordering medium. Afterwards, the condensate returns to the evaporator thanks to capillary force caused by surface tension and meniscus curvature of vapour-liquid interface.

Since the past decades, several investigations are carried out to characterize the thermal performance of heat pipes regarding various wick structure and using different working fluids either experimentally or theoretically. Khrustalev and Faghri [5] developed a mathematical model of heat and mass transfer in a micro-heat pipe. The model details the thermal characteristics depending mainly on liquid charge and input heat load. They studied liquid flow in the triangular shape of the heat pipe evolving the variation of free liquid surface curvature and interfacial shear stresses caused by interfacial vapour-liquid internal interaction. Zhu and Vafai [6] presented a two-dimensional analytical model for low-temperature porous wick cylindrical heat pipes. The vapour and liquid velocity and pressure distributions are predicted for the first time using a closed-form solution incorporating liquid-vapour interfacial hydrodynamic coupling and non-Darcian transport through the porous wick. The obtained results incorporate the steady-state vapour and wall temperatures for different input heat loads in the evaporator zone and a convective boundary condition in the condenser region. Kim et al. [7] investigated analytically and experimentally the operational characteristics and the thermal optimization of a miniature heat pipe with a grooved wick structure. The thermal performance characteristics including the effects of shear stress at the liquid-vapor interface, the initial liquid charge and the contact angle are predicted using a novel method called a modified Shah method. Lefèvre and Lallemand [8] studied an analytical solution for heat wall conduction considering a hydrodynamic model in the heat pipe. Results present wall temperature distribution, liquid and vapour isobars and velocities and maximum heat transfer capability. Chen et al. [9] developed a thermal resistance network for heat pipe system including a detailed evaporator region and calculated with traditional 1Q and Q2D methods. Their study included wall thickness effects calculations and analyse and show that the 1D method is acceptable once the heat spreading effect is limited and the Q2D method can reach about 10% error for calculating thermal resistance. Wang et al. [10] investigated

experimentally the effect of wick structure on the performance of flat plate pipes including narrow grooves and interlaced channels. The results present the thermal performance of the heat pipes axially and radially for different heat loads. Mahdavi et al. [11] conducted experiments on cylindrical copper-water heat pipe. The results detail the effect of input heat level, declination angle and working fluid volume on the temperature distribution and equivalent thermal resistance. Jafari et al. [12] examined the capillary performance of a porous structure for two-phase heat transfer especially in heat pipes application. The established range of experimental methods quantifies the capillary performance which allows the performance characterization of the heat pipe. Qu et al. [13] studied experimentally heat transfer performance and start-up characteristics of a porous-based flat-plate oscillating heat pipe and compared to the conventional one at vertical position. Results show a significant reduction in start-up temperature and the evaporator temperature decreased in heat input ranging from 60W to 180 W. Yet, the addition of sintered porous wick couldn't reach ultra-high heat flux capabilities.

Several experimental and analytical heat pipes investigations are carried out using forced convection at the condenser zone, while limited studies focus on fins based condenser with natural convection. Ye et al. [14] studied heat pipes with parallel vertical fins heat sink to manage LED case temperature under 70°C. Fins spacing was investigated and the optimum vertical spacing was predicted affording (8°C) less case temperature. The optimized thermal design was manufactured and tested experimentally which showed a good agreement between prediction and experiment. Sharifi et al. [15] presented a thermal resistance model of the heat pipe-fin array systems. They showed that heat dissipation is limited by heat transfer from the heat pipe condenser to the ambient air. They also evolved contact thermal resistance effect on thermal performance of the heat pipe using the model developed. More existing studies focus on the optimization of fins shape and spacing for enhancing heat transfer performance either associated with single phase or two phase cooling devices [16].

Yet, heat pipes can be classified into three main categories in terms of size: (i) conventional heat pipes (usual size), (ii) miniature heat pipes and (iii) micro heat pipes. Vasiliev et al [17] suggested that cylindrical and flat heat pipes with a hydraulic diameter of 1-6 mm are considered as miniature heat pipes. Besides, they showed that the classification criterion relies on the comparison of less dimension of vapor channel cross-section, meniscus curvature radius and the liquid capillary constant defined as $l_{c,HP}$:

-Microheat pipe $r_c \leq d_v < l_c$

-Miniheat pipe $r_c < d_v \leq l_c$

-Heat pipe of usual dimension $r_c < l_c < d_v$

Where l_c the capillary constant of fluid:

$$l_c = \sqrt{\frac{\sigma}{g(\rho_l - \rho_v)}}$$

Hence, the current study outlines miniature heat pipes performance as they are considered to be more adequate for electronic application comparing to the other categories. Therefore, it is relevant to improve miniature heat pipe's length as an important parameter for shape optimization of the heat pipe to be integrated in electronics cooling with less clutter while keeping good performance. Hence, studying the effect of length enables evaluating heat transfer in the heat pipe and deducing whether reducing adiabatic length doesn't affect drastically heat pipe's performance (thermal resistances, Operating temperature, liquid/vapor pressures and meniscus radius)

In this paper, the thermal performance of two porous wick flat heat pipes are experimentally investigated. Effect of heat pipe adiabatic length, tilts and various heat loads are evolved. The experimental study provides a good data base for evaporation and condensation heat transfer predictions. Indeed, the experimental heat transfer coefficients for condenser and evaporator have been shown to be the most influencing parameters on heat transfer and heat pipe thermal resistance. Thus, heat transfer coefficients are deduced from experimental results and compared to existing correlations. New correlations of phase change heat transfer are proposed basing on the experimental results. Thus, thermal model aims to predict the heat pipe thermal resistances and operating temperature taking into account the effect of porous media parameters as porous media particles radius, porosity and permeability. The obtained results are matching the experimental results of the two heat pipes. Afterwards, a mathematical model of the hydraulic behaviour of the porous wick heat pipe is developed. Also, the hydraulic model has been analysed and validated using results of Kaya and Goldak [18] hydraulic model. A parametric study of the models is also evolved by studying the effect of porosity, heat pipe adiabatic length and heat load effect on the hydrothermal behaviour of the heat pipes.

2. Experimental investigations

2.1. Experimental set up

Figure 1 shows the experimental apparatus used to run the experimental tests and measurements to evaluate heat transfer in heat pipes. It incorporates mainly a test section (1) where heat is applied to the evaporator zone of the heat pipe using a cylindrical heat cartridge of 350 W maximum power connected to a DC power supply (2) of 0 to 220 V output voltage ± 0.5%. This connection is established by means of a programmable power meter (3) within a measurement range from 1mW to 8 kW ±1 % in order to control the heat load to simulate the amount of heat generated by an electronic card. The heat pipe is instrumented with multiple micro-thermocouples ± 0.1°C (4)

welded on the upper surface of the heat pipe. The heating block is also instrumented with two rows of seven thermocouples of 1 mm diameter. The temperature measurements are recorded using an acquisition system (5). It comprises mainly a national instrument compact DAQ USB chassis for small, portable sensor measurement systems compound of two NI-9213 high-density thermocouple input modules. This system controls the timing, synchronization, and data transfer from thermocouples modules to the computer where the data is analyzed and recorded. Hence, a user interface using LabVIEW software is developed for data acquisition and signals processing which enables temperatures representation into graphs. Temperatures plot allow evaporator dry-out detecting and displaying transient and steady state from temperature curvature evolution.

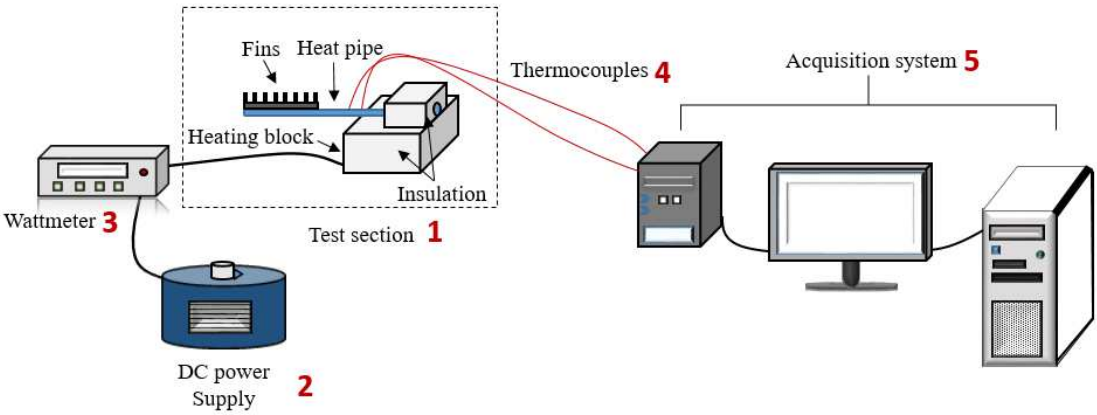

Figure 1. Schematic diagram of the experimental set up.

Before launching the experiments, the heat pipe is filled using the filling system presented in figure 2. It consists mainly of Kd Scientific syringe of ± 0.5% precision filled with working fluid. A stainless steel tubes of 0.8 mm internal diameter are connected using brass connectors. The set of valves is applied to prevent air leakage and insure a fair precision of the injected filling volume. The vacuum pump enables establishing vacuum in the filling system before filling process. Once vacuum is set within a value of 0.102 bar measured by the pressure sensor in all the system while heat pipe is heated, the working fluid is injected into the heat pipe within a speed of 1 ml/min. Then, the stainless-steel tube linked to the heat pipe is mashed using pliers then cut and covered with a thermal resistant glue to prevent leaks.

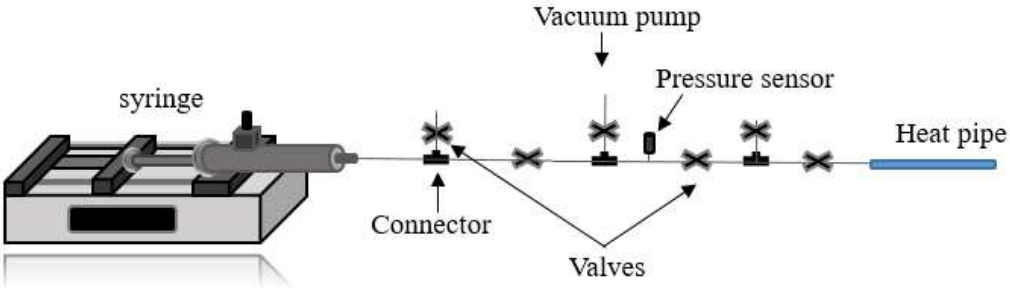

Figure 2. Schematic diagram of the filling system.

More details of the experimental set up are presented in the previous work [19] including the test bench components, filling system and process including precision and uncertainties.

2.2 Heat pipe instrumentation and uncertainties:

The studied flat porous heat pipes with different lengths present the geometrical characteristics shown in table 1.

Table 1: characteristics of the heat pipes

Properties	Heat pipe 1	Heat pipe 2
Length (mm)	225x10.5x4.5	150x10.5x4.5
Evaporator length (mm)	30	30
Condenser length (mm)	95	95
Adiabatic length (mm)	100	25
L_{eff} (mm)	200	87.5

The two heat pipes have been instrumented with the same number of thermocouples as shown in figure 3. For heat pipe (1) 4 micro thermocouples are welded on the upper surface of the condenser, while 5 at the adiabatic zone then 2 at the evaporator with an internal thermocouple of 1 mm diameter and 17 mm deep. Meanwhile, heat pipe (2) is instrumented with 5 micro thermocouples at the condenser, 2 at the adiabatic zone and 4 at the evaporator besides an internal thermocouple for vapour temperature measurement.

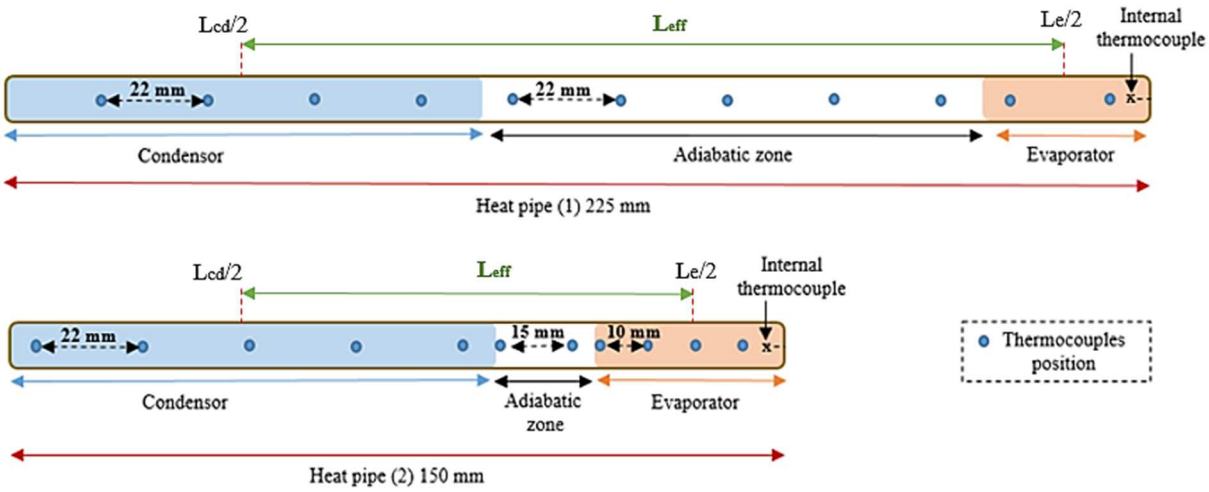

Figure 3. Thermocouples position in the two heat pipes.

The heat pipes are degassed using a vacuum pump. A selected volume of N-pentane is charged into the heat pipe via the filling system within ambient temperature. The fill ratio is about 25% as it is experimentally investigated in the previous work [19] for heat pipe (1) and is demonstrated in this paper for heat pipe (2). At various heat loads, temperatures are recorded since the start of the heating process in order to study the startup and steady state for each case. Thermocouples calibration is carried out by comparing their responses to high precision sensor probe. Table 2 presents the uncertainties of different measurement parameters.

Table 2: Uncertainties of different parameters

Parameters	Uncertainty
Temperature, T (°C)	±0.1 °C
Heat load, Qi (W)	±1%
Locations and distance (mm)	± 0.5
Thermal resistance, R(°C/W)	±1%
Fill charge	±0.5%

3. Mathematical formulation

3.1. Hydraulic model

Heat transfer performance in a heat pipe is mainly related to the heat transfer capability [20]. In sintered porous wick heat pipes, the working fluid circulates from the condenser to the evaporator thanks to the capillary pressure generated by the porous media. Therefore, the capillary pressure is calculated by the Laplace-Young equation (6).

The liquid film curvature radius is related to the capillary pressure that is variable along the axial direction from the condenser end to the evaporator end. It is a function of liquid and vapour pressures flows in the heat pipe evaporative, condensation and adiabatic zones. The curvature of the interfacial meniscus radius is defined by Laplace-Young equation as:

$$\frac{dP_v}{dz} - \frac{dP_l}{dz} = -\frac{\sigma}{{R_m}^2(z)} \frac{dR_m(z)}{dz} \tag{6}$$

The liquid pressure drop through the porous wicks is defined as:

$$\frac{dP_l}{dz} = \mu_l \frac{\dot{m}_l(z)}{\rho_l \, \mathrm{K} \, A_l} - \rho_l g sin(\alpha) \tag{7}$$

Where A_l is the wick cross sectional area. The fraction of the cross section available for the liquid flow is given by [21] as the wick is assumed to be completely saturated with liquid:

$$A_l = \frac{\pi}{4}(D_{hin} - D_{hv})^2 \epsilon \tag{8}$$

D_{hin} is the internal hydraulic diameter and D_{hv} is the vapour core hydraulic diameter, they are calculated as the following:

$$D_{hin} = 2\frac{(\mathrm{w} - 2e_w)(\mathrm{t} - 2e_w)}{(\mathrm{w} + \mathrm{t} - 4\, e_w)} \tag{9}$$

Where w and t are the width and height of the heat pipe respectively and e_w represents the thickness of heat pipe walls.

$$D_{hv} = \frac{2w_v t_v}{(w_v + t_v)} \tag{10}$$

w_v and t_v are the width and height of the vapour core respectively.

The permeability K depends mainly on the porous media's geometry and porosity. Numerous authors [22] have studied porous media permeability and the classical permeability-porosity relation is Kozeny-Carman equation used in various fields [23]. Table 3 relates the most accurate permeability prediction in literature adapted with the current study conditions.

The vapour pressure loss is defined as the sum of viscous, volume and inertial pressure losses. It is defined as

$$\frac{dP_v}{dz} = -\mu_v \frac{2(fRe)_v}{D_{hv}^2} U_v - \rho_v g \, sin(\alpha) - \frac{d}{dz}(\rho_v \beta U_v^2) \tag{15}$$

Where U_v is the average vapour flow velocity, β represents the vapor moment coefficient equal to 1.44 for laminar vapour flow [28]. The vapor friction factor-Reynolds number factor$(fRe)_v$is predicted by many authors [29-30]. In this study, $(fRe)_v$ is estimated for laminar flow by Hagen-Poiseuille equation [30].

$$f = \frac{64}{Re} \tag{16}$$

Table 3: permeability correlations

Authors	Correlations	Eq.
Rahli et al. [24]	$K = \frac{(2r_s)^2\epsilon^3}{36x10\,(1-\epsilon)^2}$	(11)
Nemec [25]	$K = \frac{r_s^2\epsilon^3}{37.5(1-\epsilon)^2}$	(12)
Bourbie ´et al. [26]	$K = C\varepsilon^n\,(2r_s)^2$	(13)
Subedi et al. [27]	$K = \frac{(2r_s)^2\epsilon^3}{122\,(1-\epsilon)^2}$	(14)

2.1.1 The mass balance equation

The heat pipe is defined by three zones: the evaporation zone($0 \le z \le L_e$), the adiabatic zone($L_e \le z \le L_e + L_a$), and the condensation zone ($L_e + L_a \le z \le L_t$). For two-phase counter-current flow, the condensate mass flow rate leaving heat pipe condensation zone at each location z should be balanced by the vapor mass flow rate arriving at the same location:

$$\dot{m}_l(z) = -\dot{m}_v(z) = \frac{-Q(z)}{h_{lv}} \tag{17}$$

The local vapour mass flow rate is defined as:

$$\dot{m}_v(z) = \rho_v U_v A_v \tag{18}$$

A_v is the vapour cross sectional area given by:

$$A_v = \frac{\pi}{4}(D_{hv})^2 \tag{19}$$

The local liquid mass flow rate of condensed vapour is given by:

$$\dot{m}_l(z) = \rho_l A_l U_l \tag{20}$$

The wick is considered to be fully saturated with liquid and is calculated by multiplying the section zone by the fractional void of the wick.

The distribution of vapour and liquid mass flow rates along the heat pipe is not uniform due to its dependence to the distribution of the heat pipe heat flux $Q(z)$in the condensation and evaporation zones. The axial distribution of heat flux is defined as

$$Q(z) = \frac{Q_i z}{L_e}, \qquad 0 \le z \le L_e \tag{21}$$

$$Q(z) = Q_i, \qquad L_e \le z \le L_e + L_a \tag{22}$$

$$Q(z) = \frac{Q_i(L_e + L_a + L_{cd} - z)}{L_{cd}}, \qquad L_e + L_a \le z \le L_e + L_a + L_{cd} \tag{23}$$

Where Q_i is the electrical heat load.

3.2. Thermal model

Reaching the optimal performance of heat pipes requires considering various design parameters such as geometry and wick structure properties, working fluid properties, operating temperature and pressure. A first approach developed by Chi [31] and widely used in the literature, consists on developing models for predicting heat pipe performance and characterizing wick structure as wick flow resistances. Poplaski and Faghri [32] analysed the internal and external thermal resistances of porous heat pipes including the integration of equivalent resistance when using fins in a three-dimensional numerical simulation. Qu et al. [33] studied the start-up characteristics and heat transfer performance of porous-based flat heat pipe experimentally and showed that sintered porous wicks cannot achieve enough high heat flux capabilities.

In the present study, internal and external thermal resistances are involved including the evaporation and condensation thermal resistances, wick and walls thermal resistance and finally the fins thermal resistance. Figure 4a shows schematic of a sintered non-circular heat pipe including fins on the condenser external heat exchange surface. The heat pipe with a hydraulic diameter D_{hout} heated with a uniform input heat is considered. The saturated pure vapor flow produced in the evaporator flows to the condenser where it condenses yielding heat to the air ambient through fins placed at the external condenser side. The condensate film leaves the condenser and flows to the evaporator zone through the microporous layers. The axial evaporator and condenser thermal resistances are not taken into consideration in the following study as they are nearly negligible for heat pipe performance.

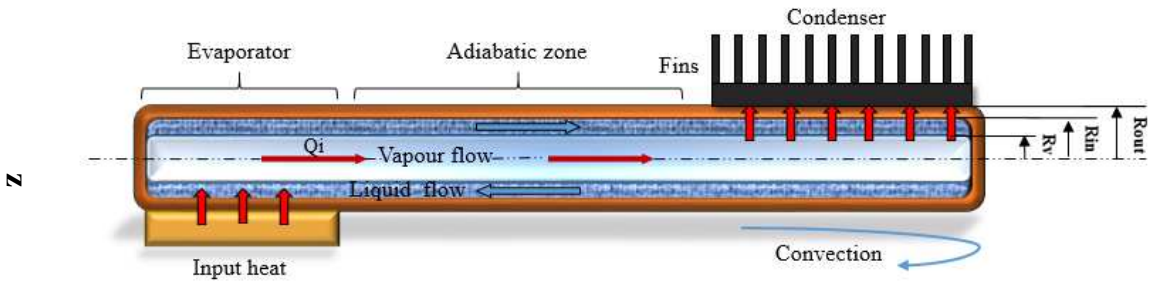

(a)

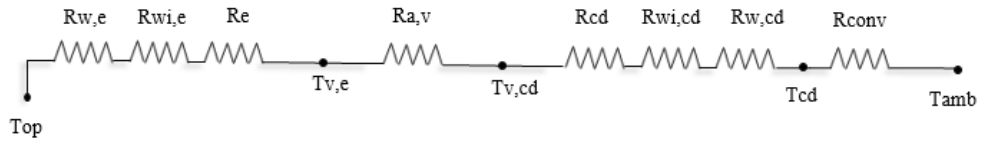

(b)

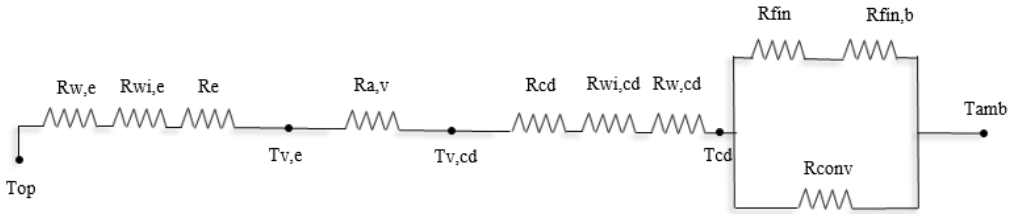

(c)

Figure 4. A sintered heat pipe with fins on the condenser: (a) schematic structure, (b) thermal resistance network of a heat pipe without fins, (c) thermal resistance network of a heat pipe with fins.

The estimation of steady state temperatures and heat flux is based on evaluating thermal resistances. As shown by figure 4b, the operating temperature for the heat pipe working without fins, could be determined from the following equation

$$T_{op} = T_{amb} + Q_i \, R_{th,sys} \tag{24}$$

The system thermal resistance represented in figure 4b is calculated by:

$$R_{th,sys} = R_{w,e} + R_{wi,e} + R_e + R_{a,v} + R_{w,cd} + R_{wi,cd} + R_{cd} + R_{conv} \tag{25}$$

When the fins are integrated at the condenser zone as presented in figure 4c, the $R_{th,sys}$ is given as:

$$R_{th,sys} = R_{w,e} + R_{wi,e} + R_e + R_{a,v} + R_{w,cd} + R_{wi,cd} + R_{cd} + \frac{R_{conv}\,(R_{fin,b} + R_{fin})}{R_{conv} + R_{fin,b} + R_{fin}} \tag{26}$$

The evaporator thermal resistance (R_e) results from a serie of three thermal resistances: the evaporator wall thermal resistance ($R_{w,e}$), the evaporator wick thermal resistance ($R_{wi,e}$), and the evaporation thermal resistance (R_e)

The evaporator wick radial thermal resistance is defined as

$$R_{wi,e} = \frac{\ln(\frac{D_{hin}}{D_{hv}})}{2\,\pi\,\lambda_{eff}\;L_e} \tag{27}$$

The wick effective thermal conductivity λ_{eff} has been commonly investigated through various models within saturated porous media [34]. The following table presents some of the predicted effective thermal conductivity [35-36]. The effective thermal conductivity is calculated for this study using eq. (29).

The evaporator wall radial thermal resistance is calculated using the following equation:

$$R_{w,e} = \frac{\ln(\frac{D_{hout}}{D_{hin}})}{2\,\pi\,\lambda_w\,L_e} \tag{28}$$

Table 4: Correlations of effective thermal conductivity

Authors	Correlations	Eq.
Hlavačka [37]	$\lambda_{eff} = \lambda_l \frac{2\lambda_l + \lambda_s - 2(1-\varepsilon)(\lambda_l - \lambda_s)}{2\lambda_l + \lambda_s + 2(1-\varepsilon)(\lambda_l - \lambda_s)}$	(29)
Faghri [38]	$\lambda_{eff} = \frac{\lambda_l\,[\lambda_l + \lambda_s - (1-\varepsilon)(\lambda_l - \lambda_s)]}{[\lambda_l + \lambda_s - (1-\varepsilon)(\lambda_l - \lambda_s)]}$	(30)
Maxwell [39]	$\lambda_{eff} = \frac{\lambda_l\,[3\lambda_s + 2(\lambda_l - \lambda_s)\varepsilon]}{[3\lambda_l - \varepsilon\,(\lambda_l - \lambda_s)]}$	(31)
Ranut [40]	$\lambda_{eff} = 0.25\,[\lambda_l\,(3\varepsilon - 1) + 3\lambda_s(1-\varepsilon) - \lambda_s + \sqrt{(\lambda_l\,(3\varepsilon - 1) + 3\lambda_s(1-\varepsilon) - \lambda_s)^2 + 8\lambda_s\lambda_l}$	(32)

The adiabatic zone is the subject of three thermal resistances resulting from axial heat conduction through the wall ($R_{w,a}$), wick ($R_{wi,a}$) and vapour ($R_{a,v}$). The adiabatic wall and wick adiabatic thermal resistances could be neglected [9].

The axial vapour flow thermal resistance in the heat pipe is due the pressure loss between evaporation and condensation zone, leading to the vapour temperature change. This resistance is defined by [41]

$$R_{a,v} = \frac{0.5L_e + L_a + 0.5L_{cd}}{0.25\,\pi\,D_{hv}^4} \frac{8\,R_g\,\mu_v\,T_e^2}{h_{lv}^2\,p_v\rho_v} \tag{33}$$

The condenser thermal resistance (R_{cd}) is equivalent of an assembly of three principal thermal resistances: the condenser wall thermal resistance$R_{w,cd}$, the condenser wick thermal resistance $R_{wi,cd}$ and the condensation thermal resistanceR_{cd}. The condenser wall thermal resistance resulting from radial heat conduction is

$$R_{w,cd} = \frac{\ln(\frac{D_{hout}}{D_{hin}})}{2\,\pi\,\lambda_w\,L_{cd}} \tag{34}$$

The condenser wick thermal resistance controlling condenser radial heat transfer is defined as

$$R_{wi,cd} = \frac{\ln(\frac{D_{hin}}{D_{hv}})}{2\,\pi\,\lambda_{eff}\,L_{cd}} \tag{35}$$

The thermal resistances for a finned heat pipe condenser surface is shown in figure 4c considering N_{fins} fins and air convection heat transfer around the fins and at the lower face of the heat pipe. Three thermal resistances are defined: the first one is resulted from the convection at the lower condenser external surface and the ambient, the second resistance of radial and axial heat conduction in the dissipater wall basis, the third resistance concerning heat

transfer through N_{fins} fins. The contact resistance between the fins basis and the heat pipe condenser is negligible due to the use of a high thermal conductivity thermal paste. The condenser basis fin thermal resistance through normal direction of heat transfer is estimated by:

$$R_{fin,b} = \frac{t_b}{W_b\ L_{bf}\ \lambda_{fin}} \tag{36}$$

Where t_{basis} and W_{basis} is the thickness and width of the fins basis plate, k_{fin} is the fins thermal conductivity.

In general, for a fin of any shape, fin thermal resistance can be written in terms of fin efficiency [42]

$$R_{fin,cd} = \frac{1}{(h_{air}\,\eta_{fin}\,N_{fin}\,A_{fin})} \tag{37}$$

h_{air} the air heat transfer coefficient, η_{fin} is the condenser fins efficiency that is determined from McAdams [43] :

$$\eta_{fin} = \left(L_{fin}\sqrt{\frac{2\,h_{air}}{\lambda_{fin}t_{fin}}}\right)^{-1} \tanh\left(L_{fin}\sqrt{\frac{2\,h_{air}}{\lambda_{fin}t_{fin}}}\right) \tag{38}$$

h_{air} is be correlated basing on the experimental measurements [44] as:

$$h_{air} = \frac{\lambda_{air}}{S_f}\left(5.5Re_{air}^{-0.133}Pr_{air}^{1/3}\right) \tag{39}$$

Re_{air} is the air Reynolds number [44] defined as:

$$Re_{air} = 2S_f\ U_{air}/\nu_{air} \tag{40}$$

V_{air} is the air velocity which is estimated around 0.1 m/s in indoor.

The convection thermal resistance at the lower surface of the condenser of the heat pipe is calculated by eq.(41)

$$R_{conv} = \frac{1}{(h_{air}\,W_b\,L_{bf})} \tag{41}$$

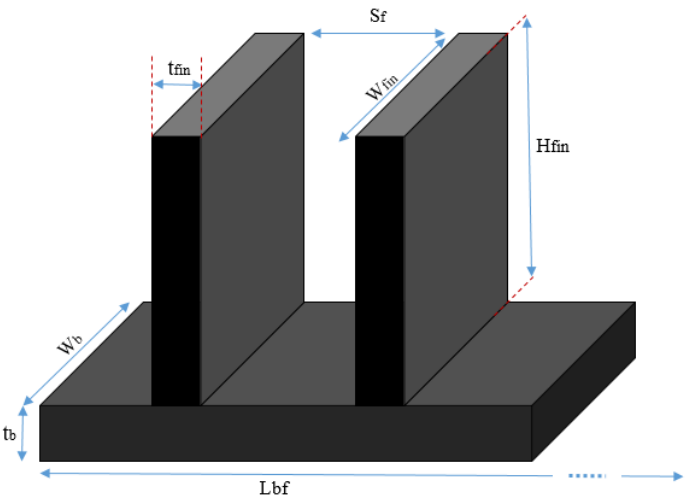

Figure 5. Schematic of the fins used at the heat pipe condenser.

3.3. Computational procedure

For a given heat load Q_i and operating temperature, distribution of the capillary pressure should be estimated for each z location along the heat pipe.

The governing equations of momentum, energy and mass conservation besides Laplace-Young equation combined with the physical boundaries' conditions are solved numerically using the fourth-order Runge-Kutta method under steady state heat transfer condition as the vapor temperature is assumed to be constant and the wick is assumed to be saturated with liquid. The capillary radius at the evaporator end cap is considered to be the minimum and is expressed in terms of effective wick particles radius and the cosine of the contact angle of the working fluid with the wick material. The liquid-vapour meniscus radius of the capillary flow inside the heat pipe could be predicted.

Assuming that the liquid-vapor interface touches the heat pipe bottom surface at z=0, the minimum liquid-vapor meniscus radius at the evaporator end cap $(z = 0)$ is geometrically defined for porous media as

$$R_{m,min} = \frac{R_{eff}}{cos(\theta)} \tag{42}$$

At z=0 liquid and vapor pressure are considered as the following:

$$P_v(\mathrm{z} = 0) = P_{sat} \tag{43}$$

$$P_l(\mathrm{z} = 0) = P_v(\mathrm{z} = 0) - \frac{2\sigma}{R_{m,min}} \tag{44}$$

A FORTRAN program is developed for step by step calculation of the evolved parameters. To start the calculations, input heat load, wick properties, heat pipe size, and working fluid nature are specified. At each step, all parameters are calculated particularly, the liquid and vapour pressure drop, the meniscus curvature radius, and liquid and vapor velocity .The calculation stops once position (z) reaches the end cap of condenser which equals to total length of the heat pipe.

4. Results and discussion

The conducted experimental tests aim to study the heat pipe adiabatic length effect on cooling performance by characterizing the thermal performance of each heat pipe and afford a sufficient database for hydraulic and thermal model validation. Measured vapour pressure and temperature, temperatures difference distribution along the heat pipe and heat pipe thermal resistance are conducted for various input heat loads. Then, tilt parameter impact on thermal performance and temperature's distribution is evolved regarding various input heat flux.

Temperature measurements are carried out throughout transient and steady state while the experimental data reduction relies on steady state. During experimental tests, steady state is reached once vapor temperature and heat

pipe walls temperature variation is comprised in ±1 °C. In most of the tests, it is noticed that temperatures deviation respects this condition after 7000s while using N-pentane as working fluid at optimal fill ratio as it is presented in the previous work [19].

4.1. Experimental results

4.1.1 Thermal characterisation

The optimal filling ratio was investigated by comparing thermal resistances of various volumes as it was detailed in the previous work [19]. It is shown that 25 % represents the optimal filling ratio corresponding to the lowest system thermal resistance. The thermal resistance variation is due mainly to two reasons: the first occurs at low input heat load, when the capillary pumping insufficiency keeps the condensate unable to return to the evaporator at low input power and causes thermal resistance increase. Whereas the second appears at increasing heat loads causing dry-out at the evaporator zone which increases thermal resistance.

Using the optimal filling ratio, the impact of adiabatic length is evolved through comparison between system thermal resistance of the heat pipe 1 of 225 mm length and heat pipe 2 of 150 mm length. Figure 6 illustrates the heat pipes thermal resistance. The system thermal resistance is used as an index for the cooling device performance. It is defined as the heat pipe thermal resistance including the operating (used as the contact temperature) and the ambient temperatures.

$$R_{th,sys} = \left(T_{op} - T_{amb}\right)/Q_i \tag{45}$$

Heat pipe 1 (La= 100 mm) reaches low thermal resistance values at increasing input heat load till the minimum of 4.79 °C/W at 12W while heat pipe 2 (La=25 mm) lowest thermal resistance is about 5.21 °C/W at 8W. Thus, increasing the heat pipe adiabatic length influences the heat flux capacity as longer heat pipes work efficiently with import heat fluxes unlike smaller heat pipes. For small heat loads, the two heat pipes keep the same thermal performance as the thermal resistances remain the same which means that length has no impact on thermal performance for small heat loads.

Both heat pipes have nearly the same behavior at low heat loads as they are not working as an effective phase change cooler but instead more as a thermal conductor throughout conduction thermal resistances. The amount of input heat flux is not sufficient to allow complete evaporation of working fluid. Therefore, vapor pressure is too low which results in inadequate condensate and insufficient liquid capillary pumping from the condenser to the evaporator for heat removal. Hence, temperatures rise drastically producing higher thermal resistances which are approximatively the same for both heat pipes as the effect of low heating condition overcomes on the variation of

adiabatic length. Since, the length of condenser and evaporator and wick structure are kept the same for the two heat pipes, the obtained wick thermal resistance and wall thermal resistance are which leads to approximately the same system thermal resistances at low heat loads.

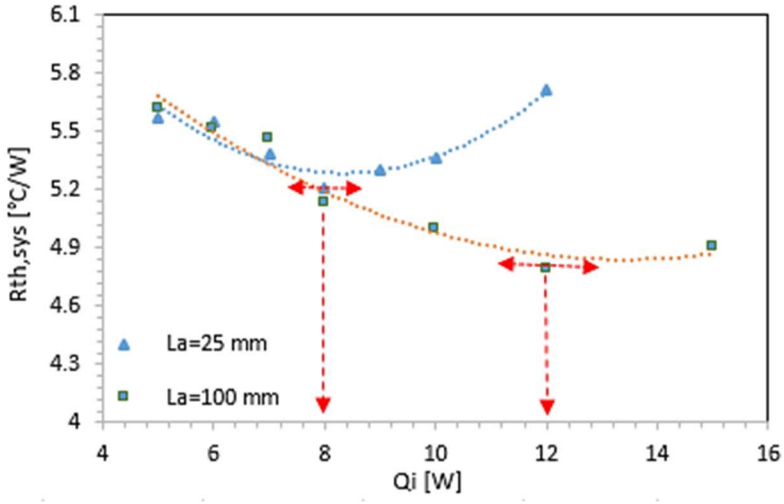

Figure 6. Experimental thermal resistances of heat pipes at horizontal position for La= 25 mm and La= 100mm.

More thermal characterization is detailed in figures 7-8 through temperatures and pressure measurement representation. Figure 7 represents vapour temperature and pressure versus heat load for the two heat pipes. The vapor temperature has been measured thanks to an internal thermocouple set inside the heat pipe at the evaporator end cap to avoid disrupting the normal functioning of the heat pipe Fig.3. Once the heat pipes perform at good conditions, the vapor is assumed to be saturated and not overheated. Hence, the pressure is deduced using saturated vapor N-pentane pressure based on the measured vapor temperature.

Since the heat capacity for La=25 mm is lower, vapour pressure and temperatures are higher comparing to La=100 mm. This is also demonstrated in figure 8 where difference temperature $\Delta T = T\text{-}T_{amb}$ distribution along the heat pipe 2 shows higher temperatures along the heat pipe 2 (La=25mm) at the same heat loads comparing to heat pipe1 (La=100mm) which means that cooling performance are enhanced for increased adiabatic length. Besides, ΔT profile in Fig.8 is explained by the fact that temperatures at the evaporator are higher since this section is being set on the heating source, then temperatures decrease slightly at the adiabatic zone and are kept constant till the condenser zone where heat is removed to the ambiance through the fins causing remarkable decrease in temperature.

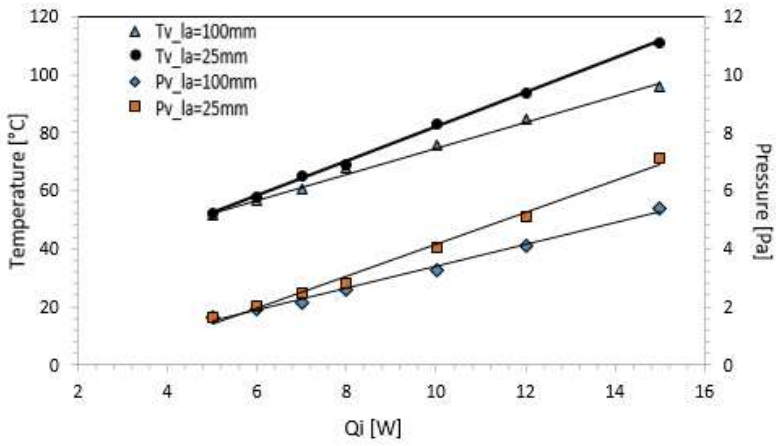

Figure 7. Measured vapor pressure and temperature for La=25 mm and La=100mm.

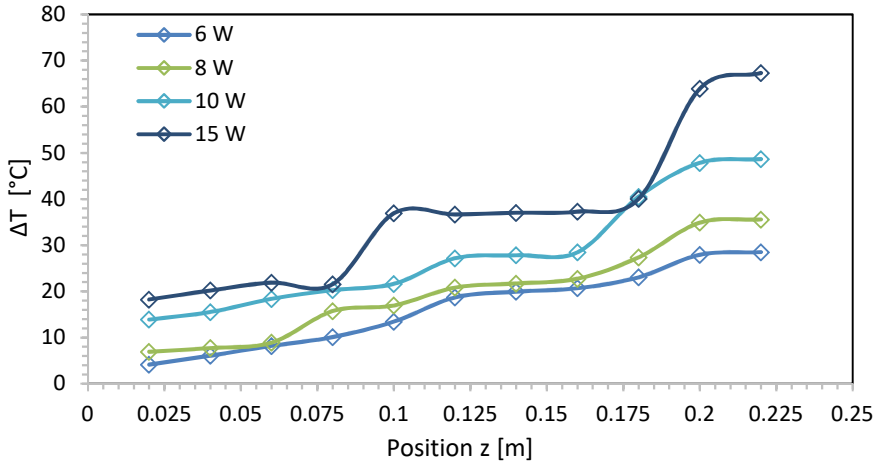

(a)

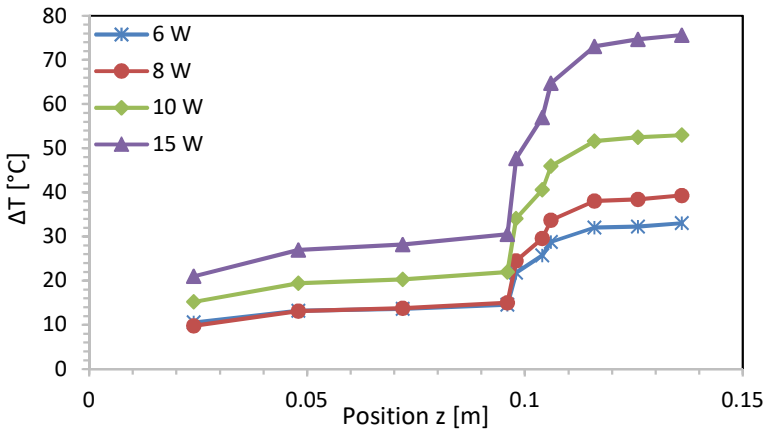

(b)

Figure 8. Distribution of heat pipe temperature for difference for: (a) La= 100 mm, (b) La=25 mm.

Tilt factor is an important parameter which influences capillary pressure inside the heat pipe. Figure 9 represents heat pipe thermal resistance versus various tilt values including horizontal position for adiabatic length of La= 25

mm. Experimental results show that tilt has not an impact on thermal resistance ($R_{th,sys}$) except horizontal position since thermal resistance is kept nearly constant and this is due to capillary forces dominating on the gravity forces. Yet, at horizontal position, thermal resistances are noticed to be lower thanks to the horizontal position that facilitates vapour circulation with less vapour/liquid friction. Also, the condenser performance is affected by fins orientation. Thus, inclining the heat pipe leads to fins orientation changing. Yet, since the fins are straight shaped the horizontal position allows more heat transfer with ambiance.

Difference temperature distribution along the heat pipe Figure 10 upholds the previous results as heat pipe at horizontal position functions at lowest temperatures comparing to inclined orientation. Also, temperatures are almost superimposed for various tilts which stands for the same thermal performance without any remarkable tilt impact.

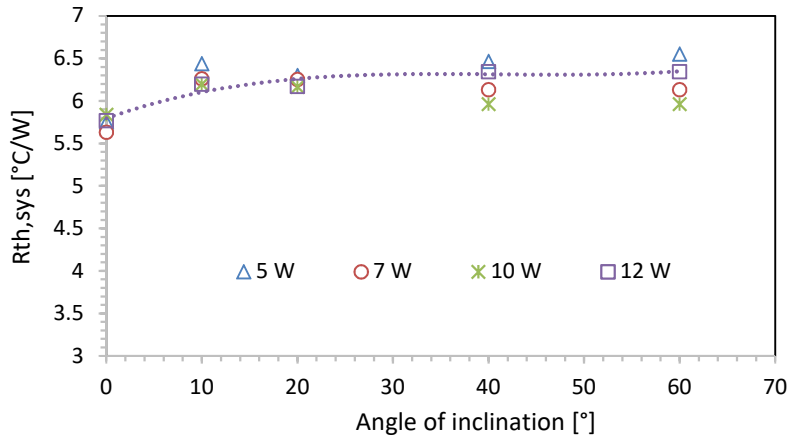

Figure 9. System thermal resistance for different tilts and heat loads for La= 25 mm

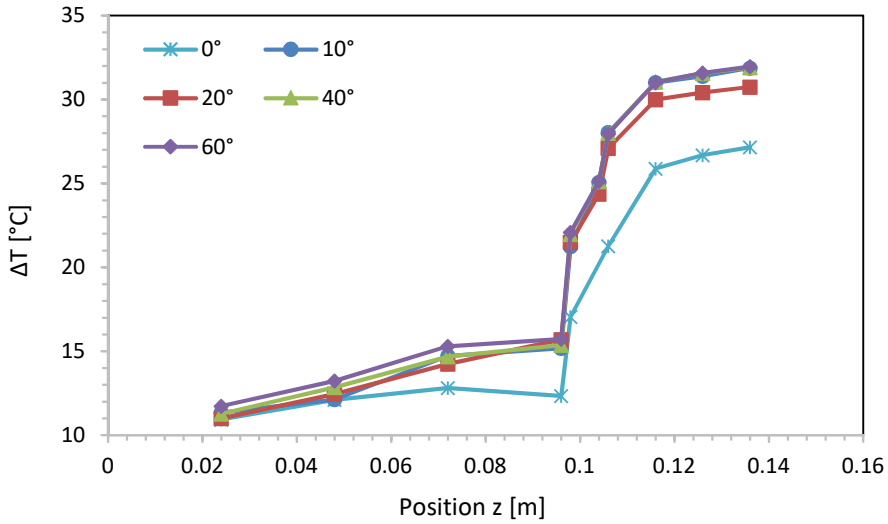

Figure 10. Temperature distribution along the heat pipe for La= 20 mm at 5W for different tilts.

4.1.2. Heat pipe evaporation heat transfer coefficient

At the beginning, it is pertinent to mention here that there aren't enough detailed studies available for calculating two-phase heat transfer coefficient for evaporation and condensation inside a porous heat pipe based on the proposed thermal resistance network analysis. The empirical correlations are provided for the prediction of condensation and evaporation heat transfer coefficient in two phase thermosyphons and others for prediction of interfacial heat transfer coefficient through porous media. Since, both are approaching the phase change phenomenon inside the heat pipe, they were used to predict heat transfer inside the heat pipe.

In this study, the chosen correlations predict heat transfer during evaporation and condensation at the same range of the obtained heat transfer coefficient from experimental results. The relative mean deviation between the selected correlations and experimental results is the lowest comparing to other authors' correlations when heat flux is comprised in [5w;10w]. Dry-out is reached once heat flux exceeds 10 W that's why there is a considerable divergence at 12 W and 15W since this model doesn't predict heat transfer when dry-out occurs. Including 12W and 15 W aim to evaluate heat transfer experimentally and discern dry-out phenomenon rather predicting it.

Hence, numerous correlations have been proposed in the literature to estimate evaporation heat transfer coefficient in porous media for several conditions as presented in table 5, yet no explicit expression is available for sintered heat pipe evaporation heat transfer coefficient. Most of these correlations consider porosity and particles size effect on heat transfer through Reynolds number considering the particles diameter as [45-46-47]. As related by Kotresha et Gnanasekaran [48], there is no explicit expression available for evaluating the evaporation heat transfer coefficient for a porous media.

In this work, using the experimental measurements, the sintered evaporation heat transfer coefficient is deduced from the total evaporator thermal resistance ($R_{e,t}$) through the following equations

$$h_e = \frac{1}{(R_{e,t} - R_{w,e})\, A_e} \tag{46}$$

Where h_e is the evaporation heat transfer coefficient and A_e is the evaporator area which can be calculated as:

$$A_e = 2(w_{v+}t_v)l_e \tag{47}$$

The evaporator thermal resistances are defined as:

$$R_{e,t} = \left(T_{ct} - T_{v,e}\right)/Q_i \tag{48}$$

Figure 11 shows the measured and estimated evaporation heat transfer coefficient versus heat flux where different existing correlations are evaluated. The given comparison shows that most of the presented correlations under-predict the measured values for the heat flux range.

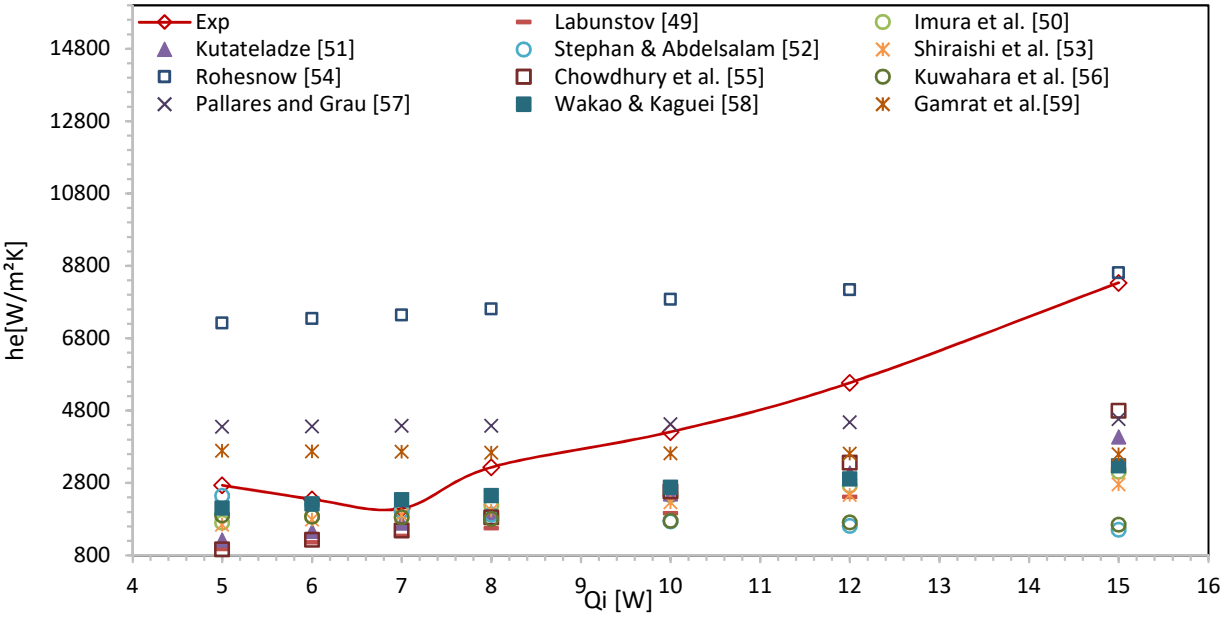

Figure 11. Evaporation heat transfer coefficient for different correlations.

Table 5: Correlations of evaporation heat transfer coefficient

Authors	Correlation	Eq.
Labunstov [49]	$he = 0.075\, q^{0.67}\left[1 + 10\left(\frac{\rho_v}{\rho_l-\rho_v}\right)^{0.67}\right]\left[\frac{\lambda_l^2}{\vartheta_1\sigma(T+273.15)}\right]^{0.33}$	(49)
Imura et al. [50]	$he = 0.32\left(\frac{\rho_l^{0.65}\lambda_l^{0.3}c_{pl}^{0.7}g^{0.2}}{\rho_v^{0.25}h_{lv}^{0.4}\mu_l^{0.1}}\right)\left(\frac{p_v}{p_{atm}}\right)^{0.3}q^{0.4}$	(50)
Kutateladze [51]	$he = 0.44\, Pr^{0.35}\left(\frac{\lambda_l}{L_b}\right)\left(\frac{\rho_l}{\rho_l-\rho_v}\,\frac{qP\times 10^{-4}}{\rho_v g h_{lv}\mu_l}\right)^{0.7}$	(51)
Stephan & Abdelsalam [52]	$he = 0.23\left(\frac{\lambda_l}{d_b}\right)\left(\frac{qd_b}{\lambda_l T_e}\right)^{-0.74}\left(\frac{h_{lv}d_b^2}{\alpha_l^2}\right)^{0.371}\left(\frac{\alpha_l^2\rho_l}{\sigma d_b}\right)^{0.35}\left(\frac{\rho_v}{\rho_l}\right)^{0.297}\left(\frac{\rho_l-\rho_v}{\rho_l}\right)^{-1.73}$	(52)
Shiraishi et al. [53]	$he = 0.32\left(\frac{\rho_l^{0.65}\lambda_l^{0.3}Cp_l^{0.7}g^{0.2}}{\rho_v^{0.25}h_{lv}^{0.4}\mu_l^{0.1}}\right)\left(\frac{P_v}{P_{atm}}\right)^{0.23}q^{0.4}$	(53)

Rohesnow [54]	$h_{Nusselt} = 1.47\ Re_l^{-1/3}(\frac{\rho_l(\rho_l-\rho_v)g\lambda_l^3}{\mu_l^2})^{1/3}$	(54)
Chowdhury et al. [55]	$he = 11.43\ (Re_b)^{0.72}Pr_l^{0.42}\left(\frac{\rho_v}{\rho_l}\right)^{0.5}(\frac{d_b}{D_{in}})(\frac{\lambda_l}{d_b})$	(55)
Kuwahara et al. [56]	$he = \left[\left(1+\frac{4(1-\varepsilon)}{\varepsilon}\right)+\frac{1}{2}(1-\varepsilon)^{1/2}Re_d^{0.6}Pr^{1/3}\right]\frac{\lambda_l}{d_b}$	(56)
Pallares & Grau [57]	$he = \left[2\left(1+\frac{4(1-\varepsilon)}{\varepsilon}\right)+(1-\varepsilon)^{1/2}Re_d^{0.6}Pr^{1/3}\right]\frac{\lambda_l}{d_b}$	(57)
Wakao & Kaguei [58]	$he = (2+1.1Re_d^{0.6}Pr^{\frac{1}{3}})\frac{\lambda_l}{d_b}$	(58)
Gamrat et al. [59]	$he = (3.02(1-\varepsilon)^{0.278}\exp(2.54(1-\varepsilon))+((1-\varepsilon)^n+0.092)Re_d^{0.5}Pr^{\frac{1}{3}}))\frac{\lambda_l}{d_b}$	(59)

The proposed correlation is based on two ranges of heat flux. For low heat flux, less than 7 W, Stephan and Abdelsalam [52] correlation accomplishes best prediction of the experimental results. Thus, the correlation is modified to predict experimental data of evaporation heat transfer. While for high heat flux values exceeding 7W heat transfer coefficient is well predicted by Wakao and Kaguei [58] which also has been modified for precise experimental data production. The proposed correlations for sintered miniature heat pipe evaporation heat transfer are expressed as

$$h_{e\_pred} = 0.297\ Re_d^{-0.189}\left(\frac{\lambda_l}{d_b}\right)\left(\frac{qd_b}{\lambda_l T_e}\right)^{-0.74}\left(\frac{h_{lv}d_b^2}{\alpha_l^2}\right)^{0.371}\left(\frac{\alpha_l^2\rho_l}{\sigma d_b}\right)^{0.35}\left(\frac{\rho_v}{\rho_l}\right)^{0.297}\left(\frac{\rho_l-\rho_v}{\rho_l}\right)^{-1.73} \quad (Q_i \le 7W) \qquad (60)$$

$$h_{e\_pred} = 0.99240\left(2+1.1Re_d^{0.6}Pr^{\frac{1}{3}}\right)\left(\frac{\lambda_l}{d_b}\right)\exp(0.0846Re_d) \quad (Qi > 7W) \qquad (61)$$

Predictions show good agreement with a deviation less than ±6% with measured values. Figure 12 represents deviation of the predicted evaporation heat transfer coefficient from measured values. The obtained results show that predicted values are matching those obtained experimentally.

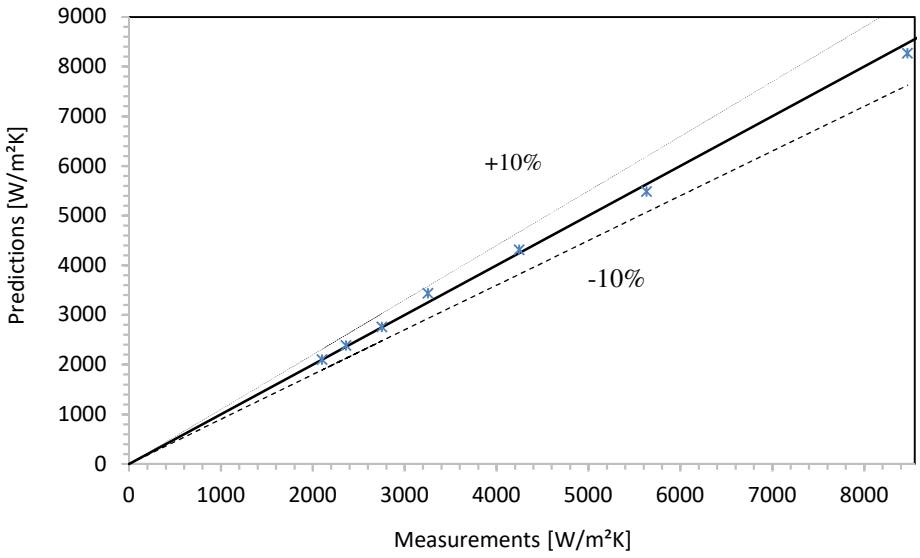

Figure 12. Evaporation heat transfer coefficient deviation.

This procedure has been also applied for predicting condensation heat transfer coefficient by comparing experimental values to the predicted ones using correlations presented in table 6. Since, no explicit expression is available for condensation heat transfer at the condenser section in miniature heat pipes, a new correlation is proposed for condensation inside the sintered miniature heat pipe. Using the experimental measurements, the condenser thermal resistance is calculated, then the measured heat transfer coefficient for condensation is deduced experimentally through the following equations:

$$h_{cd} = \frac{1}{(R_{cd,t} - R_{w,cd})\, A_{cd}} \tag{62}$$

Where h_{cd} the condensation heat transfer coefficient is estimated from the proposed correlations in the literature [46-47-60] and A_{cd} is the condenser circumferential surface which can be calculated as A_e

The evaporator and condenser thermal resistances are defined as:

$$R_{cd,t} = \left(T_{v,cd} - T_{cd}\right)/Q_i \tag{63}$$

Table 6: Correlations of condensation heat transfer coefficient

Authors	Correlation	Eq.
Nakayama et al. [61]	$\mathrm{hcd} = 0.124 \left(\frac{3\pi\varepsilon}{4(1-\varepsilon)}\right)^{0.605} (\mathrm{Re_d Pr})^{0.791} \frac{\lambda_l}{d_b}$	(64)
Zukauskas et al. [62]	$\mathrm{hcd} = 0.022\, \mathrm{Re_d^{0.84}} \mathrm{Pr}^{0.36}\, \frac{\lambda_l}{d_b}$	(65)

Chen & Wung [63]	$\mathrm{hcd} = 0.8\mathrm{Re}_d^{0.4}\mathrm{Pr}^{0.37}\,\frac{\lambda_l}{d_b}$	(66)
Kreith et al. [64]	$\mathrm{hcd} = (\frac{1-\varepsilon}{\varepsilon})(0.5\mathrm{Re}_d^{\frac{1}{2}} + 0.2\,\mathrm{Re}_d^{\frac{2}{3}})\mathrm{Pr}^{1/3}\,\frac{\lambda_l}{d_b}$	(67)
Jiang et al. [65]	$\mathrm{hcd} = (0.86 - 4.93\varepsilon + 7.08\varepsilon^2)\mathrm{Re}_d^{1.15}\mathrm{Pr}^{\frac{1}{3}}\frac{\lambda_l}{d_b}$	(68)
Calmidi & Mahajan [66]	$\mathrm{h_{cd}} = 0.52\,\mathrm{Re}_d^{0.5}\mathrm{Pr}^{0.37}\,\frac{\lambda_l}{d_b}$	(69)
Hashimoto & Kaminaga [67]	$\mathrm{hcd} = 1.25\mathrm{Re}_l^{0.1}\exp(-1.\,10^{-5}\frac{\rho_v}{\rho_l} - 0.6)\;\mathrm{Re}_l^{-1/3}(\frac{\rho_l(\rho_l-\rho_v)g\lambda_l^3}{\mu_l^2})^{1/3}\,\frac{\lambda_l}{d_b}$	(71)
Jouhara & Robinson [68]	$\mathrm{hcd} = 1.25\mathrm{Re}_l^{0.1}\exp(-1.\,10^{-5}\frac{\rho_v}{\rho_l} - 0.14)\;\mathrm{Re}_l^{-1/3}(\frac{\rho_l(\rho_l-\rho_v)g\lambda_l^3}{\mu_l^2})^{1/3}\,\frac{\lambda_l}{d_b}$	(72)

Figure 13 presents the measured condensation heat transfer coefficient versus heat flux regarding various existing correlations. The given comparison shows that most of the presented correlations over-predict the measured values except for Kreith et al.[64] correlation which is considered to be the most approaching correlation to the experimental results.

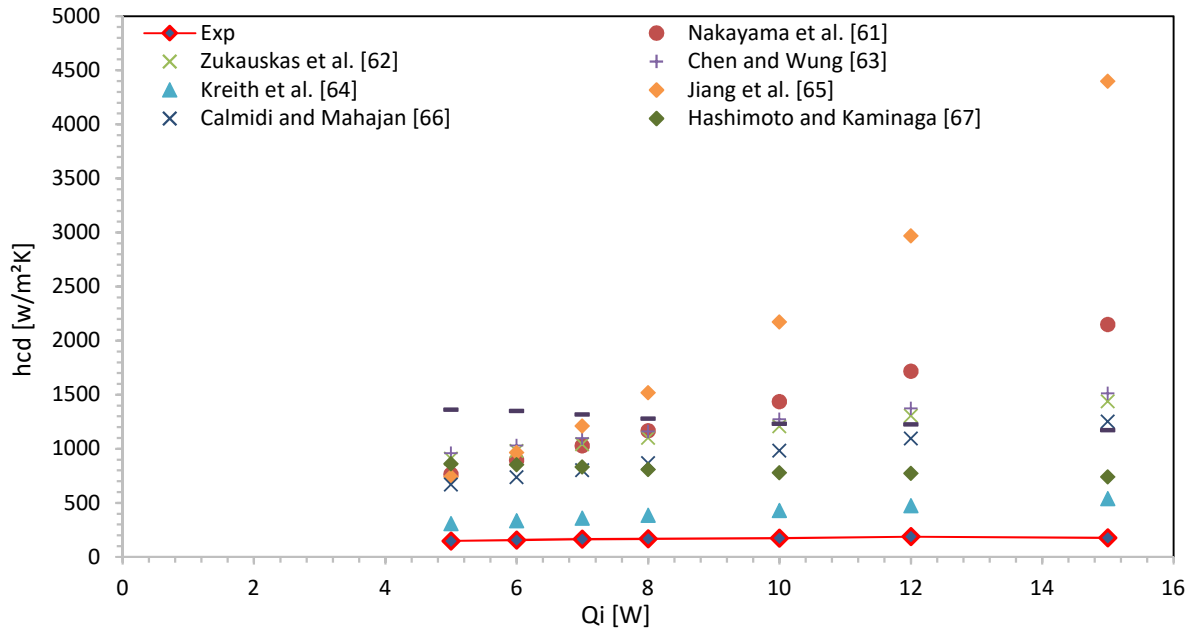

Figure 13. Condensation heat transfer coefficient for different correlations.

Kreith et al. [64] correlation is modified in this work to predict experimental data of condenser interfacial heat transfer which is expressed as the following:

$$h_{cd} = 0.585\, Re_d^{-0.219}\left(\frac{1-\varepsilon}{\varepsilon}\right)\left(0.5Re_d^{\frac{1}{2}} + 0.2\, Re_d^{\frac{2}{3}}\right)Pr^{\frac{1}{3}}\frac{\lambda_l}{d_b} \quad (73)$$

Figure 13 shows experimental and predicted condensation heat transfer coefficient for the tested sintered heat pipe. Predictions show good agreement with a deviation less than ±10% with measured values. This deviation of the predicted condensation heat transfer coefficient from measured values is presented in figure 14.

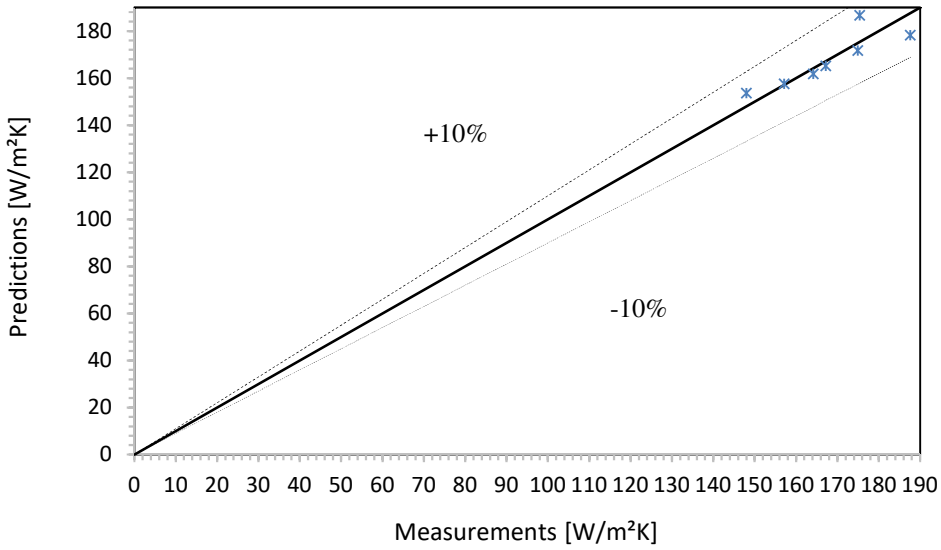

Figure 14. Condensation heat transfer coefficient deviation.

The predicted results of both evaporation and condensation thermal resistances that enable operating temperature prediction are close as presented in figures 12-14 except some discrepancy due to the assumption of uniform heat flux input and constant vapor temperature. The similar difficulty of accurately predicting heat transfer coefficient and thermal resistances based on heat pipe temperature distribution is also seen in [18] where it is stated the existence of some deviation between heat pipes temperature prediction and experimental measurement.

4.2. Modelling results

4.2.1 Verification of the predicted operating temperatures

Since the operating temperature implies the electronic heating element temperature, it is necessary to define this temperature's range for better optimization of the electronic chips cooling. The predicted and estimated operating temperatures for different input heat loads are presented for the two tested heat pipes in figures 15 and 16 regarding different heat loads. Both figures represent good agreement between experimental and measured temperatures,

except for heat pipe 2 (La= 25 mm) in which prediction starts deviating from experimental due to dry-out phenomenon which is not taken into account in the thermal model.

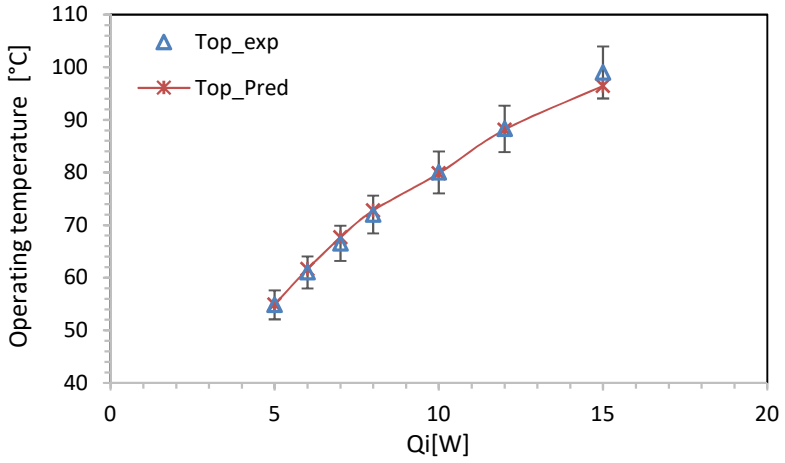

Figure 15. Operating temperature La= 100 mm.

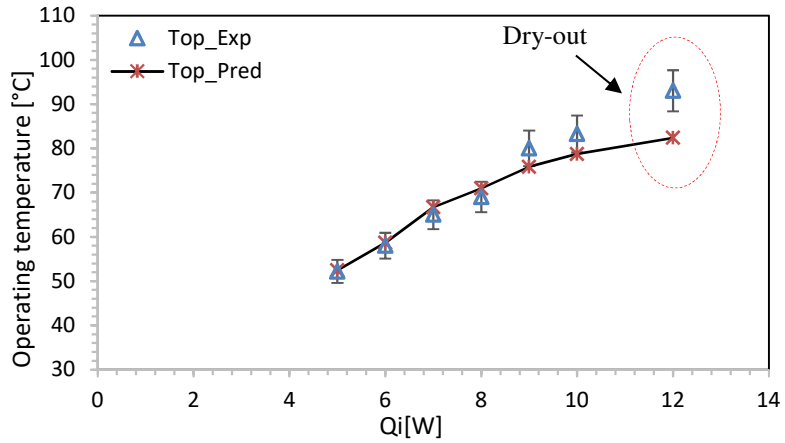

Figure 16. Operating temperature La=25 mm.

4.2.2 Verification of the predicted vapour and liquid local pressures

In order to verify the predictions of the hydraulic model, the simulations are carried out for copper porous wick heat pipe and the results are compared with those obtained by Kaya and Goldak [18]. The heat pipe is 6.35 mm outer-diameter and 220 mm long copper pipe with a 0.8 mm wall thickness. Both evaporator and condenser sections have the same length 50.8mm. The input heat load is about 20W and the working fluid temperature is set to 371K. The effective thermal conductivity is set to 1.47 W/mK while the wick permeability is about 1.93×10^{-10} m². The liquid and vapor pressures presented by the figures 17 and 18, show good agreement with those of Kaya & Goldak within

an average deviation less than 6% for vapor pressure and 12% for liquid pressure. Yet, the deviation appeared at the initial position for liquid pressure is due mainly to boundary conditions applied by Kaya & Goldak which varies from the provided boundary conditions in the present study including the assumed contact angle and the adopted effective pore radius of the wick.

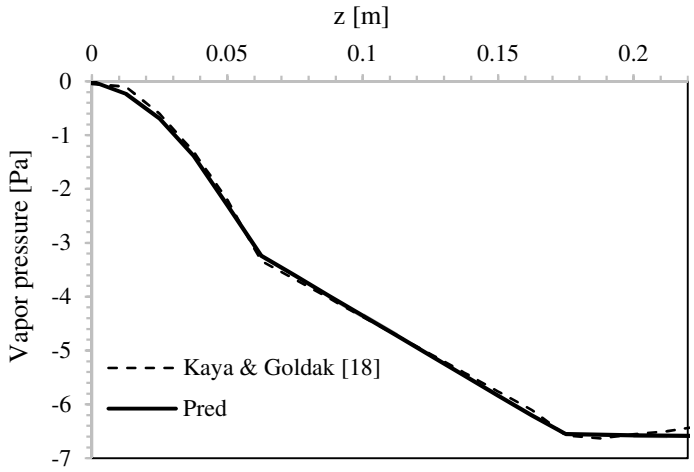

Figure 17. Vapor relative pressure at Qin=20W with natural convection cooling

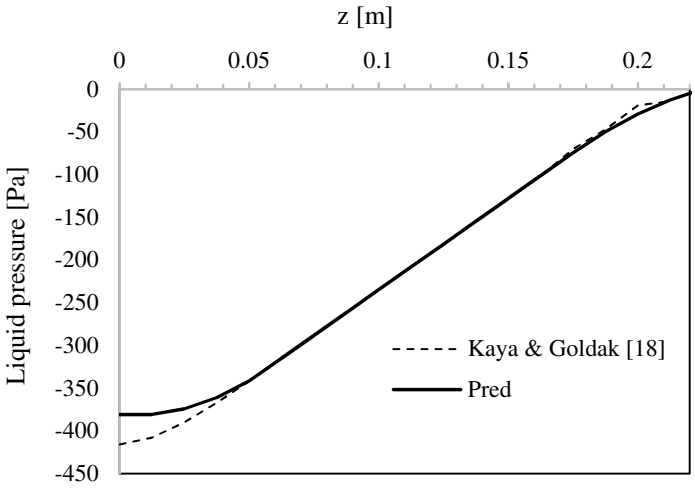

Figure 18. Liquid relative pressure at Qin=20W with natural convection cooling.

4.2.3 Impact of adiabatic length on the capillary pressure and velocity

More characterization is presented by figure 19, for heat pipe within adiabatic length of 100 mm by investigating the effect of heat load on capillary pressure. It is shown that capillary pressure is reduced with increasing heat loads since vapor pressure rises. Also, capillary pressure difference between the evaporator and condenser increases for heat loads increment. For instance, at 5 W capillary pressure is 666 Pa at (z=0) then decreases to 478 at the end of

the condenser, while at 8 W capillary pressure is around 579 Pa at (z=0) then decreases to 305 Pa at the end of the condenser. Also, Figure 20 represents capillary pressure for adiabatic lengths of 100 mm and 25mm which represents on the other hand the effect of adiabatic length on hydraulic behavior of the heat pipe. The capillary pressure reaches 561Pa for heat pipe 2 while 478Pa for La= 100 mm, these results agree with the thermal aspect since heat pipe 1 dissipates heat flux more efficiently particularly higher heat fluxes. Figure 21 also represent liquid and vapor velocity profiles for La=100mm and La=25mm which are relevant parameters related to pressure distribution. Yet, velocities are not affected at small heat loads by the length of adiabatic zone of the heat pipe since the same heat pipe characteristics are preserved including input heat load permeability and operating temperature, yet these values could vary slightly for same important heat loads applied to the two heat pipes.

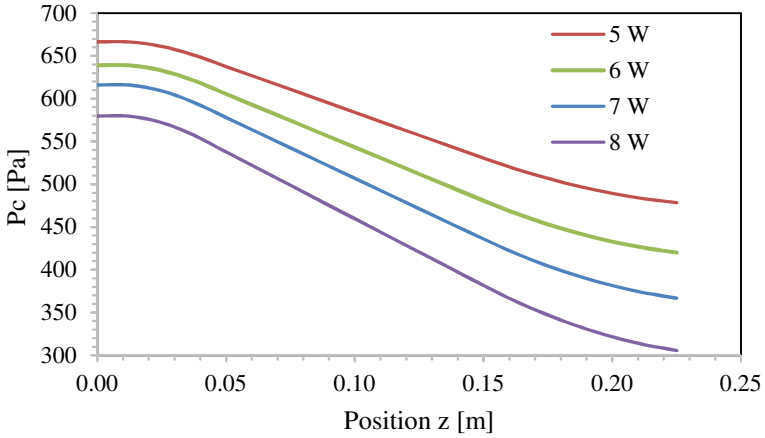

Figure19. Effect of heat load on capillary pressure at La= 100 mm.

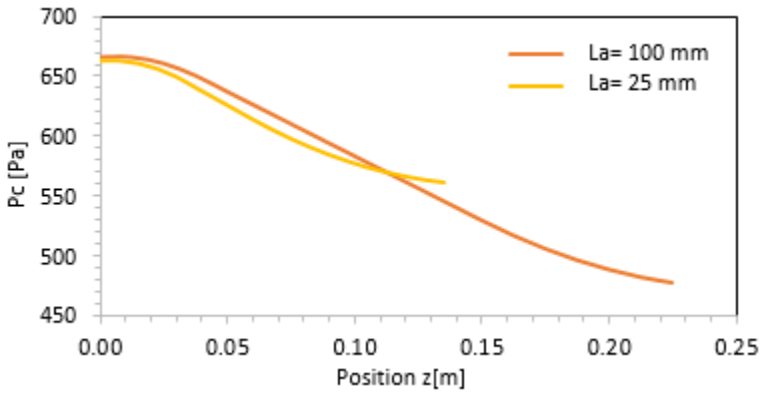

Figure 20. Capillary pressure at 5W.

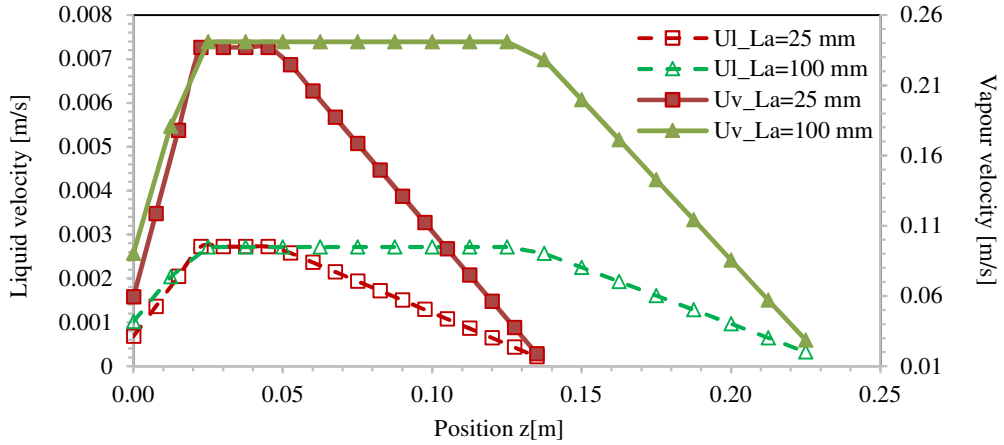

Figure 21. Liquid and vapor velocity distribution at 5W.

4.2.5 Effect of porosity material on the operating temperature

Since the studied heat pipes have a porous wick structure, some major parameters which characterize the porous media have a significant impact on heat transfer as particles size (radius of the particles as it is assumed that the particles are spherical), porosity and permeability. Therefore, operating temperature is affected by wick porosity as presented in Figure 22. In fact operating temperature decreases to an optimum porosity value then increases. Yet, this fluctuation of operating temperature decreases when the radius of particles reaches small values less than what is recommended in literature [3µm-15µm] for copper particles [21]. When, porosity decreases to smaller values the effect of capillarity is reduced which decreases the effectiveness of heat transfer in the heat pipe and thus operating temperature rises. Meanwhile, operating temperature rises for higher values of porosity due to the decrease of wick effective thermal conductivity and the increase of thermal resistance. Besides, Reducing porosity to an optimal value induces flow recirculation and increases overall heat and mass transfer [69]. Figure 23 shows the obtained optimum porosity versus particles size. As the particles radius increases, the optimum porosity decreases and stabilizes at 10% which represents the limit of porous wick structure porosity.

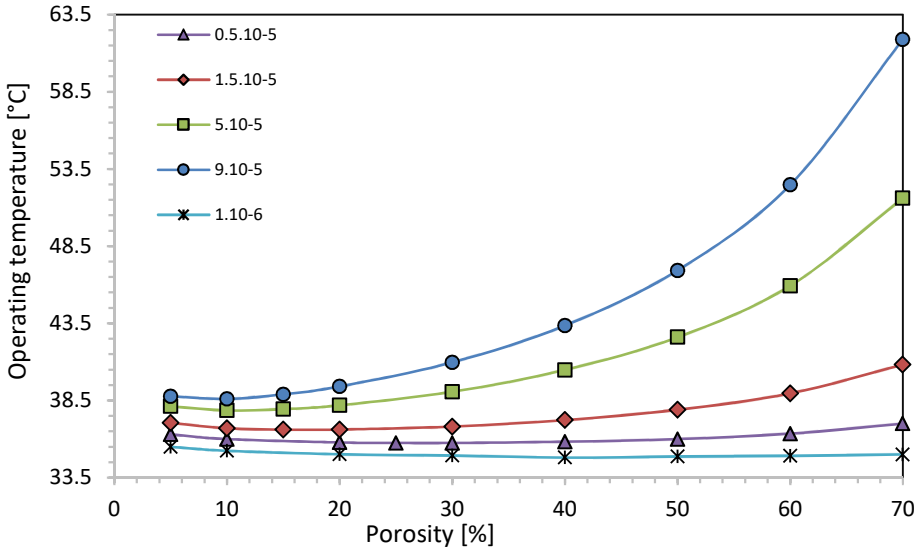

Figure 22. Effect of porosity on operating temperature at 5W.

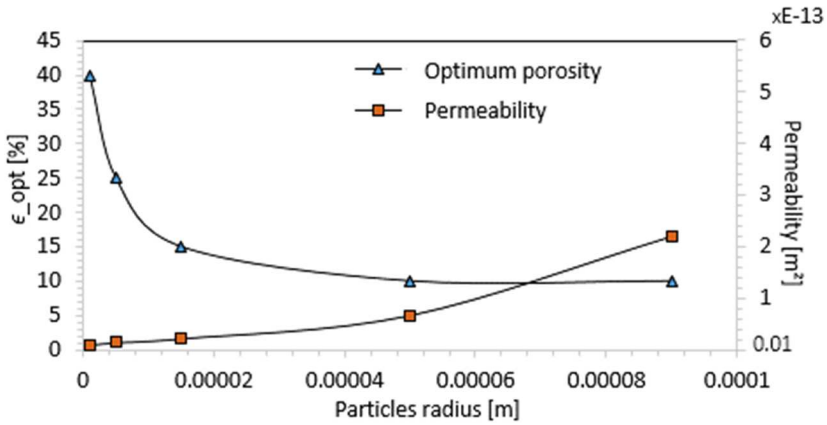

Figure 23. Impact of particles size on permeability and optimum porosity.

Conclusion

This paper investigated experimentally heat transfer of two porous wick heat pipes with different lengths including the effect of tilt. The major experimental findings are resumed in that longer is the heat pipe the higher is its transport capacity. For smaller heat loads Qi≤ 7W, the heat pipe keeps the same heat transfer performance regarding different adiabatic lengths and also miniature heat pipes work efficiently at horizontal position while thermal performance remains the same for tilts [10°:60°].

A thermal analysis is conducted by predicting a new correlation of heat transfer in porous media in the evaporation and condenser zone which enables a good estimation of operating temperature. An extended study of the porous wick particles size and porosity show that there has been an optimum value of porosity comprised between 10 %

and 40 % regarding different particles size which affords the lowest operating temperature. Permeability increases too when particles radius increases and remains almost constant for particles radius lower than 1 μm.

This work incorporates also a hydraulic mathematical model that shows a good agreement with Kaya's. The increase of heat load and adiabatic length reduces the capillary pressure while increasing porosity increases liquid pressure without any significant impact on capillary pressure.

6. Acknowledgement

This work is conducted under CobBauge project selected by the European cross-border cooperation program INTEREG V France (Manche)-England. The authors would like to thank ERDF for the funding of this work.

References

[1] Faghri, A. Review and advances in heat pipe science and technology. Journal of heat transfer, 134(12), 123001 (2012).

[2] Schlitt, R. Evolution of heat pipe technology for satellite application. In 10th International Heat Pipe Conference (1997) (p. 2).

[3] Riehl, R. Utilization of passive thermal control technologies for electronics cooling: a brief review. *Journal of Applied Mechanical Engineering*, 5, (2016) 214.

[4] Yang, X., Yan, Y. Y., & Mullen, D. Recent developments of lightweight, high performance heat pipes. *Applied Thermal Engineering*, 33, (2012) 1-14.

[5] Khrustalev, D., & Faghri, A. Thermal analysis of a micro heat pipe. *Journal of Heat transfer*, 116(1), (1994) 189-198.

[6] Zhu, N., & Vafai, K. Analysis of cylindrical heat pipes incorporating the effects of liquid–vapor coupling and non-Darcian transport—a closed form solution. *International Journal of Heat and Mass Transfer*, 42(18), (1999) 3405-3418.

[7] Kim, S. J., Seo, J. K., & Do, K. H. Analytical and experimental investigation on the operational characteristics and the thermal optimization of a miniature heat pipe with a grooved wick structure. *International Journal of Heat and Mass Transfer*, 46(11), (2003) 2051-2063.

[8] Lefevre, F., & Lallemand, M. Coupled thermal and hydrodynamic models of flat micro heat pipes for the cooling of multiple electronic components. *International Journal of Heat and Mass Transfer*, 49(7-8), (2006) 1375-1383.

[9] Chen, S. W., Chiu, W. J., Lin, M. S., Kuo, F. J., Chai, M. L., Lee, J. D., ... & Shih, C. 1D and Q2D thermal resistance analysis of micro channel structure and flat plate heat pipe. *Microelectronics Reliability*, 72, (2017) 103-114.

[10] Wang, C., Liu, Z., Zhang, G., & Zhang, M. Experimental investigations of flat plate heat pipes with interlaced narrow grooves or channels as capillary structure. *Experimental Thermal and Fluid Science*, 48, (2013) 222-229.

[11] Mahdavi, M., Tiari, S., De Schampheleire, S., & Qiu, S. Experimental study of the thermal characteristics of a heat pipe. *Experimental Thermal and Fluid Science*, 93, (2018) 292-304.

[12] Jafari, D., Wits, W. W., & Geurts, B. J. Metal 3D-printed wick structures for heat pipe application: Capillary performance analysis. *Applied Thermal Engineering*, 143, (2018) 403-414.

[13] Qu, J., Sun, Q., Wang, H., Zhang, D., & Yuan, J. Performance characteristics of flat-plate oscillating heat pipe with porous metal-foam wicks. *International Journal of Heat and Mass Transfer*, 137, (2019) 20-30.

[14] Ye, H., Li, B., Tang, H., Zhao, J., Yuan, C., & Zhang, G. Design of vertical fin arrays with heat pipes used for high-power light-emitting diodes. *Microelectronics Reliability*, 54(11), (2014) 2448-2455.

[15] Sharifi, N., Stark, J. R., Bergman, T. L., & Faghri, A. The influence of thermal contact resistance on the relative performance of heat pipe-fin array systems. *Applied Thermal Engineering*, 105, (2016) 46-55.

[16] Meng, X., Zhu, J., Wei, X., & Yan, Y. Natural convection heat transfer of a straight-fin heat sink. *International Journal of Heat and Mass Transfer*, 123, (2018) 561-568.

[17] Vasiliev, L. L., Kulakov, A. G., Filatova, O. S., & Epifanov, S. V. Copper sintered powder wick structures of miniature heat pipes. In VI Minsk international seminar 'heat pipes, heat pumps, refrigerators. Minsk, Belarus (2005) 12-15.

[18] Kaya, T., & Goldak, J. Three-dimensional numerical analysis of heat and mass transfer in heat pipes. *Heat and Mass Transfer*, 43(8), (2007) 775-785.

[19] Zeghari, K., Louahlia, H., & Le Masson, S. Experimental investigation of flat porous heat pipe for cooling TV box electronic chips. *Applied Thermal Engineering*, (2019) 114267.

[20] Faghri, A. (1995). Heat pipe science and technology. Global Digital Press (1995).

[21] Reay, D., McGlen, R., & Kew, P. (2013). Heat pipes: theory, design and applications. Butterworth-Heinemann. (2013).

[22] Xu, P., & Yu, B. Developing a new form of permeability and Kozeny–Carman constant for homogeneous porous media by means of fractal geometry. *Advances in water resources*, 31(1), (2008) 74-81.

[23] Cho, S. H., Colin, F., Sardin, M., & Prost, C. Settling velocity model of activated sludge. *Water Research*, 27(7), (1993) 1237-1242.

[24] Rahli, O., Tadrist, L., Miscevic, M., & Santini, R. Fluid flow through randomly packed monodisperse fibers: The Kozeny-Carman parameter analysis. *Journal of Fluids Engineering*, 119(1), (1997) 188-192.

[25] Nemec, P., Čaja, A., & Malcho, M. Mathematical model for heat transfer limitations of heat pipe. *Mathematical and Computer Modelling*, *57*(1-2), (2013) 126-136.

[26] Bourbie´T, Coussy O, Zinszner B. Acoustics of porous media. Par-is: Educ Technol; (1987).

[27] Subedi, B., Kim, S. H., Jang, S. P., & Kedzierski, M. A. Effect of mesh wick geometry on the maximum heat transfer rate of flat-micro heat pipes with multi-heat sources and sinks. *International Journal of Heat and Mass Transfer*, 131, (2019) 537-545

[28] HOPKINS, R., FAGHRI, A., et KHRUSTALEV, D. Flat miniature heat pipes with micro capillary grooves. (1999).

[29] Awad, M. M. Prediction of wall friction factor in horizontal annular flow using the asymptotic method. *Annals of Nuclear Energy*, 65, (2014) 308-313.

[30] Bharathan, B., McGuinness, M., Kuhar, S., Kermani, M., Hassani, F. P., & Sasmito, A. P. Pressure loss and friction factor in non-Newtonian mine paste backfill: Modelling, loop test and mine field data. *Powder technology*, 344, (2019) 443-453.

[31] Chi, S. W. Heat pipe theory and practice. Washington, DC, Hemisphere Publishing Corp.; New York, McGraw-Hill Book Co., (1976) 256 p.

[32] Poplaski, L. M., Faghri, A., & Bergman, T. L. Analysis of internal and external thermal resistances of heat pipes including fins using a three-dimensional numerical simulation. *International Journal of Heat and Mass Transfer*, 102, (2016) 455-469.

[33] Qu, J., Sun, Q., Wang, H., Zhang, D., & Yuan, J. Performance characteristics of flat-plate oscillating heat pipe with porous metal-foam wicks. *International Journal of Heat and Mass Transfer*, 137, (2019) 20-30.

[34] Qin, X., Cai, J., Xu, P., Dai, S., & Gan, Q. A fractal model of effective thermal conductivity for porous media with various liquid saturation. *International Journal of Heat and Mass Transfer*, 128, (2019) 1149-1156.

[35] Qin, X., Cai, J., Xu, P., Dai, S., & Gan, Q. A fractal model of effective thermal conductivity for porous media with various liquid saturation. *International Journal of Heat and Mass Transfer*, 128, (2019) 1149-1156.

[36] Poplaski, L. M., Faghri, A., & Bergman, T. L. Analysis of internal and external thermal resistances of heat pipes including fins using a three-dimensional numerical simulation. *International Journal of Heat and Mass Transfer*, 102, (2016) 455-469.

[37] V.Hlavačka, F.Polášek, P.Štulc,V.Zbořil, Tepelné Trubicev Elektrotechnice, STNL-Nakladatelství Technické Literatúry ,Praha,(1990).

[38] Poplaski, L. M., Faghri, A., & Bergman, T. L. Analysis of internal and external thermal resistances of heat pipes including fins using a three-dimensional numerical simulation. *International journal of Heat and Mass Transfer*, 102, (2016) 455-469.

[39] Maxwell J. Wang, J.K. Carson, M.F. North, D.J. Cleland, A new approach to modelling the effective thermal conductivity of heterogeneous materials, *International Journal of Heat and Mass Transfer*. 49 (17–18) (2006) 3075–3083.

[40] P. Ranut, the effective thermal conductivity of aluminum metal foams: review and improvement of the available empirical and analytical models, *Applied Thermal Engineering* 101 (2016) 496–524.

[41] Shabgard, H., Allen, M. J., Sharifi, N., Benn, S. P., Faghri, A., & Bergman, T. L. Heat pipe heat exchangers and heat sinks: opportunities, challenges, applications, analysis, and state of the art. *International Journal of Heat and Mass Transfer*, 89, (2015) 138-158.

[42] Tardy, F., & Sami, S. M. Thermal analysis of heat pipes during thermal storage. *Applied Thermal Engineering*, 29(2-3), (2009) 329-333.

[43] W.H. McAdams, Heat Transmission, third ed., McGraw Hill Book Company, New York, 1954.

[44] Sundaram, A. S., & Bhaskaran, A. Thermal modeling of thermosyphon integrated heat sink for CPU cooling. *Journal of Electronics Cooling and Thermal Control*, 1(02), (2011) 15.

[45] Yang, P., Wen, Z., Dou, R., & Liu, X. Heat transfer characteristics in random porous media based on the 3D lattice Boltzmann method. *International Journal of Heat and Mass Transfer*, 109, (2017) 647-656.

[46] Jafari, D., Franco, A., Filippeschi, S., & Di Marco, P. Two-phase closed thermosyphons: a review of studies and solar applications. *Renewable and Sustainable Energy Reviews*, 53, (2016) 575-593.

[47] Jafari, D., Di Marco, P., Filippeschi, S., & Franco, A. An experimental investigation on the evaporation and condensation heat transfer of two-phase closed thermosyphons. *Experimental thermal and fluid science*, 88, (2017) 111-123.

[48] Kotresha, B., & Gnanasekaran, N. Determination of interfacial heat transfer coefficient for the flow assisted mixed convection through brass wire mesh. *International Journal of Thermal Sciences*, 138, (2019) 98-108.

[49] Labuntsov, D. A. Heat transfer problems with nucleate boiling of liquids. *Thermal Engineering* 19, (1973) 21-28.

[50] Imura, H., Kusuda, H., Ogata, J. I., Miyazaki, T., & Sakamoto, N. Heat transfer in two-phase closed-type thermosyphons. *JSME Transactions*, 45, (1979) 712-722.

[51] Kutateladze, S. S. Heat transfer and hydrodynamic resistance. E′ nergoatomizdat, Moscow (1990).

[52] Stephan, K., & Abdelsalam, M. Heat-transfer correlations for natural convection boiling. *International Journal of Heat and Mass Transfer, 23(1), (1980) 73-87.*

[53] M. Shiraishi, Y. Kim, M. Murakami, P. Terdtoon, A correlation for the critical heat transfer rate in an inclined two-phase closed thermosyphon, in: Proceedings of 5th International Heat Pipe Symposium, Melbourne, (1996).

[54] W.M. Rohsenow, A method of correlating heat transfer data for surface boiling of liquids, *Journal of Heat Transfer ASME* 74 (1952) 969–976.

[55] F.Md. Chowdhury, F. Kaminaga, K. Goto, K. Matsumura, Boiling heat transfer ina small diameter tube below atmospheric pressure on a natural circulation condition, *Journal of Jpn. Association Heat Pipe* 16 (1997) 14–16.

[56] F. Kuwahara, S. Mitsuhiro, A. Nakayama, A numerical study of interfacial convective heat transfer coefficient in two-energy equation model for convection in porous media, *International Journal of Heat and Mass Transfer*. 44 (2001) 1153–1159.

[57] J. Pallares, F.X. Grau, A modification of a Nusselt number correlation for forced convection in porous media, *International Communication of Heat and Mass Transfer* 37 (2010)1187–1190.

[58] N. Wakao, S. Kaguei, Heat and Mass Transfer in Packed Beds, Gordon andBreach, New York, (1982).

[59] G. Gamrat, F.M. Michel, L.P. Stephane, Numerical study of heat transfer overbanks of rods in small Reynolds number cross-flow, *International Journal of Heat and Mass Transfer* 51(2008) 853–864

[60] Yang, P., Wen, Z., Dou, R., & Liu, X. Heat transfer characteristics in random porous media based on the 3D lattice Boltzmann method. *International Journal of Heat and Mass Transfer*, 109, (2017) 647-656.

[61] Nakayama, A., Ando, K., Yang, C., Sano, Y., Kuwahara, F., & Liu, J. A study on interstitial heat transfer in consolidated and unconsolidated porous media. *Heat and Mass Transfer*, 45(11), (2009) 1365-1372.

[62] Žukauskas, A. Heat transfer from tubes in crossflow. *In Advances in heat transfer* 8, (1972) 93-160.

[63] Chen, C. J., & Wung, T. S. Finite analytic solution of convective heat transfer for tube arrays in crossflow: Part II—Heat transfer analysis. *Journal of Heat Transfer*, 111(3), (1989) 641-648.

[64] Kreith, F., Manglik, R. M., & Bohn, M. S. Principles of heat transfer. Cengage learning. (2012).

[65] Jiang, P. X., Xu, R. N., & Gong, W. Particle-to-fluid heat transfer coefficients in miniporous media. *Chemical engineering science*, 61(22), (2006) 7213-7222.

[66] Kotresha, B., & Gnanasekaran, N. Determination of interfacial heat transfer coefficient for the flow assisted mixed convection through brass wire mesh. *International Journal of Thermal Sciences*, 138, (2019) 98-108.

[67] Hashimoto, H., & Kaminaga, F. Heat transfer characteristics in a condenser of closed two-phase thermosyphon: Effect of entrainment on heat transfer deterioration. Heat Transfer—Asian Research: Co-sponsored by the Society of Chemical Engineers of Japan and the Heat Transfer Division of ASME, 31(3), (2002) 212-225.

[68] Jouhara, H., & Robinson, A. J. Experimental investigation of small diameter two-phase closed thermosyphons charged with water, FC-84, FC-77 and FC-3283. *Applied Thermal Engineering*, 30(2-3), (2010) 201-211.

[69] Carvalho, P. H., & de Lemos, M. J. . Role of porosity and solid-to-fluid thermal conductivity ratio on turbulent combined heat and mass transfer in a porous cavity. *International Journal of Heat and Mass Transfer*, 132, (2019) 221-237.